DOI: 10.13009/EUCASS2022-6193
9TH EUROPEAN CONFERENCE FOR AERONAUTICS AND SPACE SCIENCES (EUCASS)

Reusable Launchers Re-entry Controlled Dynamics Simulator

Alice De Oliveira[⋆†] *and Michèle Lavagna*[⋆]
[⋆]*Politecnico di Milano, Aerospace Science and Technology Department*
Via Giuseppe La Masa 34, 20156 Milano, Italy
alice.deoliveira@polimi.it · michelle.lavagna@polimi.it
[†]Corresponding author

Abstract

This paper focuses on the implementation of a fixed planar fins model in a Reusable Launch Vehicle (RLV) re-entry dynamics simulator with closed-loop guidance and control integration. The vehicle first-stage booster studied, evolving in the terrestrial atmosphere, is steered by a thrust vector control system correcting the trajectory deviations from the reference profile computed in real-time by a successive convex optimisation algorithm. Numerical results show that the fins model developed is viable for RLV re-entry Guidance & Control assessment and that significant vehicle's control authority can be provided by aerodynamic steering for effectively reducing trajectory deviations and enabling pinpoint landing.

1. Introduction

Over the last decade, launcher reusability has become the new paradigm for reducing the cost of access to space and for enabling future manned missions such as a return to the Moon or, even more ambitiously, the first step on Mars. This technology was already developed in the Space Shuttle era, however, unanticipated costs and risks led to the cancellation of the programme in 2011. But some years ago, private companies, such as SpaceX and Blue Origin, completely disrupted the space sector and demonstrated the cost effectiveness and technical feasibility of reusable rockets. More particularly, SpaceX's *Falcon 9* was, in 2017, the first Vertical Take-Off Vertical Landing (VTVL) vehicle having its first stage recovered after launch and reused for another mission, and then became, in 2020, the first private rocket to take astronauts to the International Space Station thanks to its cargo spacecraft *Dragon* [1]. The leading company is now successfully testing its *Super Heavy* rocket equipped with the *Starship* spacecraft with the objective to carry both crew and cargo on long-duration interplanetary flights and to make humanity return to the Moon and travel to Mars and beyond. In the meantime, Blue Origin is also developing advanced reusable launchers such as *New Shepard*, a sub-orbital launch vehicle designed for space tourism, and *New Glenn*, a heavy-lift reusable rocket which should be able to bring heavy payloads to Earth orbit and beyond [2]. Consequently, national agencies and intergovernmental institutions are following the same path, increasing research and development on launcher reusability.

Reusable Launch Vehicles (RLVs) atmospheric re-entry and precision soft-landing on Earth is very challenging, mainly due to the atmosphere presence. Indeed, during this phase, the vehicle is subjected to fast system dynamics changes induced by external loads such as lift and drag, unpredictable wind and gusts, and also to control-induced actuation commands to answer the landing constraints satisfaction, allowing the so-called pinpoint landing while preserving the vehicle's integrity. All those involve uncertainties and nonlinearities as well as coupling effects with high frequencies, which leads to vehicle's instability and therefore give reason why for a high performance Guidance, Navigation & Control (GNC) system implementation. This demanding problem became feasible in the past decade with the development of convex optimisation: a particular class of methods which allows to compute, in real-time and based on the current flight conditions, optimal trajectories to be followed satisfying desired constraints (which must be convex). This technology has been demonstrated with the Masten Space Systems' VTVL demonstrator *Xombie* which used a vision-based system and a fuel-optimal convex guidance algorithm to optimally fly towards the desired landing site [3].

Research on convex optimisation for the entry, descent and soft pinpoint landing of VTVL reusable launchers was actively carried out in the last years with the development of advanced techniques such as successive convex optimisation [4], and pseudospectral convex optimisation [5]. In Ref. [6], Liu extended this first method by combining aerodynamic forces and propulsion as control inputs to gain optimality with the consideration of the aerodynamics of the vehicle, previously ignored. Then in Ref. [7], Sagliano *et al.* combined both methods and proposed to separate the aerodynamic descent and the powered landing into two different optimal control problems, using the aerodynamic

Copyright © 2022 by Alice De Oliveira and Michèle Lavagna. Published by the EUCASS association with permission.

DOI: 10.13009/EUCASS2022-6193

forces as control inputs for the first phase, and a combination of aerodynamic and propulsive control for the second phase. Finally, in Ref. [8], Simplício *et al.* have achieved a trade-off between efficiency and optimality according to the study of the coupled flight mechanics and considered a larger flight envelope encountered by the RLV.

Indeed the coupled flight mechanics which intervene in reusable launchers re-entry are usually not considered in the design of optimal guidance algorithms. The disturbances and uncertainties acting on the vehicle and coming from the nonlinear dynamics, external events (e.g. wind, aerodynamics), the actuation system, and the environment, are counteracted thanks to a robust control system. Classic techniques involves the use of linear control theory based on the linearisation of the equations of motion and feedback of defined control parameters with gain-scheduling [9]. However, these techniques require an extensive verification and validation campaign with Monte-Carlo analyses, which renders the process very time and cost consuming. Lately, advanced robust control methods have been studied in both academia and industry, such as linear parameter varying approach [10] and the H_∞ family of methods, more particularly the *structured* H_∞ technique [11].

The steering of a VTVL reusable rocket during the atmospheric re-entry is generally mainly achieved by a Thrust Vector Control (TVC) system, which actuates by deflecting the engine's nozzle along the two body axes perpendicular to the vehicle's longitudinal axis by specific gimbal angles, computed by the control algorithm for satisfying the reference trajectory generated by the guidance. To increase the control authority of the RLV, especially at low thrust during the aerodynamic descent, steerable fins are crucial. They are placed above the vehicle's centre of pressure with usually one pair for controlling the pitch motion and another pair for controlling the yaw motion. Finally, a Reaction Control System (RCS) based on cold gas thrusters is often added to be used at high altitude in low dynamic pressure conditions. However, the aerodynamics generated by steerable fins are usually not considered in the guidance [8], or interpolated through multidimensional look-up tables, which depend on Mach number, angle of attack, sideslip angle and on the fin deflections [7]. In Ref. [12], Simplício *et al.* developed a model for planar fins implementation on a RLV controlled through their control effectiveness according to the current flight conditions and pitch and yaw deviations compared to the reference profile given by the guidance.

In this work, an approach is proposed to integrate the fins implementation into the guidance scheme, in order to evaluate their impact in the computation of the reference trajectory, and then, on the RLV re-entry dynamics simulator. A model of two pairs of planar fins, similar to the one designed by Simplício *et al.* in Ref. [12], have been developed. For this preliminary study, the fins are considered fixed and uncontrolled. Therefore, they are inserted in a RLV re-entry dynamics simulator with closed-loop guidance and control integration, which covers a VTVL vehicle first-stage booster atmospheric re-entry and soft pinpoint landing. It includes the Six-Degree-of-Freedom (6-DoF) re-entry dynamics of a rigid-body model with varying mass, evolving in the terrestrial atmosphere with varying environmental parameters, uncertainties and disturbances (atmospheric density, ambient pressure, wind), and subjected to external forces (gravity, aerodynamics). The steering of the spacecraft is carried out by a TVC system, correcting the trajectory deviations with respect to the reference profile generated by a successive convex optimisation guidance algorithm and updated several times during the flight.

The paper is organised as follows. Sec. 2 introduces the reusable launchers re-entry dynamics simulator with the description of all the building blocks of the model: from environment models and vehicle's properties to closed-loop guidance and control methods implementation. Then, in Sec. 3, the planar fins model is described and implemented in the guidance method and in the simulator. Subsequently, several simulations are performed in Sec. 4 and compared to the standard case without fins. A sensitivity analysis is carried out, modifying design parameters, to study the impact of the fins in the simulator and better address them for control implementation. Finally, conclusions and future works are provided in Sec. 5.

2. Reusable launchers re-entry dynamics simulator

The RLV re-entry dynamics simulator developed in this paper relies on the nonlinear 6-DoF dynamics of a VTVL vehicle first-stage booster modelled as a rigid body with varying mass, subjected to external forces induced by the terrestrial atmosphere and controlled through embedded closed-loop guidance and control strategies. Therefore, it is composed of several building blocks with interconnections between them. The elements have been implemented through MATLAB/Simulink and will be briefly presented in the following subsections. A performance analysis of the simulator described hereafter has been carried out in Ref. [13].

Reference frames and environment models adopted for gravity, atmospheric parameters and wind are explained in Sec. 2.1. Then, equations of motion, aerodynamics calculation, and center of gravity (CG) and inertia estimations are described in Sec. 2.2. At this stage of the RLV re-entry simulator design, the vehicle is only steered via TVC, introduced in Sec. 2.3.

Finally, the simulator is equipped with a Guidance & Control (G&C) system divided in two subsystems. The first one, the guidance algorithm, is responsible for the real-time generation of a reference trajectory to be followed by

DOI: 10.13009/EUCASS2022-6193

the vehicle with thrust and attitude commands. In this simulator, a successive convex optimisation guidance is used and the global strategy will be more detailed in Sec. 2.4. Then, the control algorithm generates the necessary commands to correct the possible deviations from the reference trajectory due to uncertainties and disturbances existing in the terrestrial atmosphere. A classic linear control theory method with gain-scheduled Proportional-Integral-Derivative (PID) controllers is used and presented in Sec. 2.5. Note that, at this stage of the RLV re-entry dynamics simulator design, no navigation system is considered meaning that it is assumed to have a direct access to the actual states of the vehicle.

2.1 Reference frames and environment models

This subsection describes the reference frames and environment models that have been adopted in the RLV re-entry dynamics simulator. They are essential to simulate the re-entry of a reusable rocket in the terrestrial atmosphere.

Two reference frames are considered. The first one is the landing site reference frame. Its origin is at the landing site and it is an Up-East-North reference frame, such that the $\mathbf{x}_I$-axis points Up, $\mathbf{y}_I$-axis East, while $\mathbf{z}_I$-axis North. This reference frame is considered inertial and the equations of motion are referred to it. The simulations are initiated from an initial position in this reference frame $\mathbf{r}_I(0)$, with an initial velocity $\mathbf{v}_I(0)$. The second reference frame is the vehicle's body-fixed reference frame. It is fixed to the vehicle's CG and the basis vectors can be defined as: $\mathbf{x}_B$-axis lies along the vehicle's longitudinal axis and $\mathbf{y}_B$-axis is defined so as to remain perpendicular to the pitch plane while $\mathbf{z}_B$-axis completes the right-handed system (and thus remains perpendicular to the yaw plane). Following those definitions, roll, pitch and yaw angles $\{\phi(t), \theta(t), \psi(t)\}$ represent the orientation of the body-fixed reference frame with respect to the landing site inertial reference frame. These angles will be useful to control the trajectory of the vehicle. However, in the formulation of the equations of motion, the rotation quaternion $\mathbf{q}_B^I(t)$ is used to translate the attitude of the vehicle to avoid the singularity caused by 90 deg of attitude. Therefore, $\mathbf{R}_B^I(t)$ represents the rotation matrix from the inertial reference frame to the vehicle's body-fixed reference frame. The angular velocity is defined in the body-fixed reference frame with an initial value $\boldsymbol{\omega}_B(0)$.

The atmosphere model adopted in this study, available in MATLAB *Aerospace Toolbox* [14], implements the mathematical representation of the 1976 Committee on Extension to the Standard Atmosphere (COESA) which allows to provide, as a function of altitude $h(t)$, the atmospheric density $\rho(h(t))$ and the pressure $P_{amb}(h(t))$. Then, the gravitational field is defined in the inertial frame by $\mathbf{g}_I(h(t)) = \begin{bmatrix} g(h(t)) & 0 & 0 \end{bmatrix}^T$ where $g(h(t))$ is obtained as a function of the altitude and expressed by:

$$g(h(t)) = g_0 \left(\frac{R_E}{R_E + h(t)} \right)^2 \tag{1}$$

where g_0 is the standard Earth gravity and R_E is the radius of the Earth. For conciseness, these values will now be written as function of the time t.

Finally, constant wind have been computed with the U.S. Naval Research Laboratory model *Horizontal Wind Model 14*, also available in Ref. [14], which generates the meridional $w_{mer}(t)$ and zonal $w_{zon}(t)$ components of the wind for a set of geophysical data. Wind gusts are modelled as a cosine-shape function, such that the user can define the amplitude of the gusts and the altitude where it happens. The function is expressed as follows:

$$\mathbf{V}_{gust}(h(t)) = \mathbf{A}_{gust} \left(1 - \cos\left(\frac{\pi(h(t) - h_1)}{0.5\Delta h} \right) \right) \tag{2}$$

where $\mathbf{A}_{gust} \in \mathbb{R}^3$ specifies the amplitude of the gust in the three directions, $h(t)$ is the current altitude of the spacecraft, h_1 specifies the altitude where the gust starts, while Δh is the altitude range in which the gust is applied. Therefore, the maximum intensity of the gust is reached in the middle of the specified altitude region. Consequently, the wind vector is written in the inertial reference frame as follows:

$$\mathbf{w}_I(t) = \begin{bmatrix} 0 & w_{mer}(t) & w_{zon}(t) \end{bmatrix}^T + \mathbf{V}_{gust}(h(t)) \tag{3}$$

Note that the wind model is not considered in the re-entry dynamics of the guidance algorithm described in Sec. 2.4.

2.2 Equations of motion, aerodynamics and CG/inertia estimations

Equations of motion are written using the reference frames previously defined in Sec. 2.1. They are based on the initial state vector $\mathbf{x}_I(0) = \begin{bmatrix} m(0) & \mathbf{r}_I^T(0) & \mathbf{v}_I^T(0) & \mathbf{q}_B^I(0)^T & \boldsymbol{\omega}_B^T(0) \end{bmatrix}$ and on the assumptions that the vehicle is a rigid body with no effects induced by the varying mass (e.g. propellant sloshing) and structural flexibilities.

DOI: 10.13009/EUCASS2022-6193

The mass depletion dynamics are modelled by an affine function of the thrust magnitude as follows:

$$\dot{m}(t) = -\frac{\|\mathbf{F}_{TVC,I}(t)\|_2}{I_{sp}g_0} - \frac{A_{nozzle}P_{amb}(t)}{I_{sp}g_0} \tag{4}$$

where I_{sp} is the vacuum specific impulse of the engine, g_0 is the standard Earth gravity, A_{nozzle} is the nozzle exit area of the engine and $P_{amb}(t)$ is the ambient atmospheric pressure. $\mathbf{F}_{TVC,I}(t) \in \mathbb{R}^3$ is the thrust vector coming from the TVC system, introduced in Sec. 2.3, represented in the inertial reference frame. The second term is related to the reduction of the specific impulse due to the atmospheric back-pressure [4].

The translational states, position and velocity of the vehicle in the inertial reference frame, $\mathbf{r}_I(t) \in \mathbb{R}^3$ and $\mathbf{v}_I(t) \in \mathbb{R}^3$, are governed by the following dynamics:

$$\begin{aligned} \dot{\mathbf{r}}_I(t) &= \mathbf{v}_I(t) \\ \dot{\mathbf{v}}_I(t) &= \frac{1}{m(t)}\left[\mathbf{F}_{TVC,I}(t) + \mathbf{F}_{aero,I}(t)\right] + \mathbf{g}_I(t) \end{aligned} \tag{5}$$

where $\mathbf{F}_{aero,I}(t) \in \mathbb{R}^3$ described the aerodynamic force acting on the vehicle in the inertial reference frame, introduced hereafter.

Then, the attitude states are governed by the following rotational dynamics, using the quaternion-based kinematics equation:

$$\begin{aligned} \dot{\mathbf{q}}_B^I(t) &= \frac{1}{2}\begin{bmatrix} q_4(t) & -q_3(t) & q_2(t) \\ q_3(t) & q_4(t) & -q_1(t) \\ -q_2(t) & q_1(t) & q_4(t) \\ -q_1(t) & -q_2(t) & -q_3(t) \end{bmatrix}\boldsymbol{\omega}_B(t) \\ \dot{\boldsymbol{\omega}}_B(t) &= J^{-1}(t)\left[\mathbf{M}_{TVC,B}(t) + \mathbf{M}_{aero,B}(t) - \boldsymbol{\omega}_B(t) \times J\boldsymbol{\omega}_B\right] \end{aligned} \tag{6}$$

where J is the inertia matrix of the vehicle, introduced hereafter. $\mathbf{M}_{TVC,B}(t) \in \mathbb{R}^3$ (Sec. 2.3) and $\mathbf{M}_{aero,B}(t) \in \mathbb{R}^3$ represent, respectively, the thrust and aerodynamic torques acting on the vehicle. In Eq. (6), the coupling between angular velocity and inertia along the three axes, and the effect of centroid movement on the inertia caused by mass consumption, are ignored.

At this stage of the RLV re-entry dynamics simulator design, a *spherical* aerodynamic model is used to describe the aerodynamics of the vehicle. This model, introduced by Szmuk *et al.* in Ref. [4], approximates the relationship between the aerodynamic force and the velocity vector and has the advantage to be easily implementable in the successive convex optimisation guidance method. The aerodynamic force $\mathbf{F}_{aero,I}(t)$ is considered always anti-parallel with respect to the air-relative velocity $\mathbf{v}_{air,I}(t)$ as if the vehicle was subjected to a pure drag force, where $\mathbf{v}_{air,I}(t) = \mathbf{v}_I(t) - \mathbf{w}_I(t)$ accounts for the wind. Therefore, assuming that the rocket is axisymmetric, the aerodynamic forces and moments in the vehicle's body-fixed reference frame are expressed by:

$$\begin{aligned} \mathbf{F}_{aero,B}(t) &= -\frac{1}{2}\rho(t)\|\mathbf{v}_{air,I}(t)\|_2 S_{ref} C_{aero}\mathbf{R}_B^I(t)\mathbf{v}_{air,I}(t) \\ \mathbf{M}_{aero,B}(t) &= [\mathbf{x}_{CP} - \mathbf{x}_{CG}(t)] \times \mathbf{F}_{aero,B}(t) \end{aligned} \tag{7}$$

where S_{ref} is the reference aerodynamic area of the vehicle, and $\mathbf{x}_{CP} = \begin{bmatrix} x_{CP} & 0 & 0 \end{bmatrix}^T$ and $\mathbf{x}_{CG} = \begin{bmatrix} x_{CG}(t) & 0 & 0 \end{bmatrix}^T$ represent, respectively, the center of pressure (CP) and the CG. C_{aero} is the aerodynamic coefficient matrix defined by $C_{aero} = \text{diag}\left(\begin{bmatrix} c_{a,x} & c_{a,x} & c_{a,x} \end{bmatrix}\right)$ where $c_{a,x}$ is a positive scalar considered assumed constant during all the flight.

Finally, because of propellant mass and level variations along the flight, the total vehicle CG and the moments of inertia are also varying. The CG is considered lying along the vehicle's body longitudinal axis such as $\mathbf{x}_{CG} = \begin{bmatrix} x_{CG}(t) & 0 & 0 \end{bmatrix}^T$ while the inertia tensor is assumed diagonal such as $J(t) = \text{diag}\left(\begin{bmatrix} J_A(t) & J_N(t) & J_N(t) \end{bmatrix}\right)$. Following the model and data available in Ref. [12], the vehicle's mass is broken down into structural mass and time-dependent propellant mass, which is updated via Eq. (4) during engine burn, as follows:

$$m(t) = m_{prop}(t) + m_{dry} \tag{8}$$

with m_{dry} the dry mass of the vehicle and $m_{prop}(t)$ the propellant mass defined as $m_{prop}(t) = m_{fuel}(t) + m_{oxid}(t)$, with $m_{fuel}(t)$ the mass of fuel and $m_{oxid}(t)$ the mass of oxidizer. Then, knowing the change over time of fuel and oxidizer masses and their level on the corresponding tanks, $h_{fuel}(t)$ and $h_{oxid}(t)$, the vehicle's CG can be computed as:

$$x_{CG}(t) = \frac{1}{m(t)}\left[m_{fuel}(t)\left(h_{tk,fuel} + \frac{h_{fuel}(t)}{2}\right) + m_{oxid}(t)\left(h_{tk,oxid} + \frac{h_{oxid}(t)}{2}\right) + m_{dry}h_{dry}\right] \tag{9}$$

DOI: 10.13009/EUCASS2022-6193

where $h_{tk,fuel}$ and $h_{tk,fuel}$ are the tank heights and h_{dry} the dry CG height. The axial component of the inertia tensor is expressed by:

$$J_A(t) = \frac{1}{2} m_{prop}(t) r_{tk}^2 + J_{A,dry} \tag{10}$$

where r_{tk} is the tank radius and $J_{A,dry}$ the axial component of the inertia tensor of the dry vehicle. Then, the lateral component of the inertia tensor is given by:

$$\begin{aligned} J_N(t) = J_{N,fuel}(t) + J_{N,oxid}(t) + J_{N,dry} + m_{fuel}(t)\left(h_{tk,fuel} + \frac{h_{fuel}(t)}{2} - x_{CG}(t)\right)^2 \\ + m_{oxid}(t)\left(h_{tk,oxid} + \frac{h_{oxid}(t)}{2} - x_{CG}(t)\right)^2 + m_{dry}(h_{dry} - x_{CG}(t))^2 \end{aligned} \tag{11}$$

where $J_{N,dry}$ is the lateral component of the inertia tensor of the dry vehicle and the lateral contributions of the propellant masses relative to their CG, $J_{N,fuel}(t)$ and $J_{N,oxid}(t)$ are expressed by:

$$J_{N,fuel}(t) = \frac{1}{2} m_{fuel}(t)(3r_{tk}^2 + h_{fuel}^2(t)) \tag{12}$$

$$J_{N,oxid}(t) = \frac{1}{2} m_{oxid}(t)(3r_{tk}^2 + h_{oxid}^2(t)) \tag{13}$$

2.3 Thrust Vector Control system

The trajectory of the vehicle during the descent is controlled by adjusting the magnitude and the direction of the thrust vector generated by the main engine. It is achieved with the TVC actuator by deflecting the engine's nozzle by $\beta_{TVC,y}(t)$ and $\beta_{TVC,y}(t)$, respectively along the $\mathbf{y}_B$-axis and the $\mathbf{z}_B$-axis. The required thrust magnitude $T_{ref}(t)$ and deflection angles $\{\beta_{TVC,y}(t), \beta_{TVC,z}(t)\}$ are obtained, from the guidance algorithm (2.4) and the control method (2.5) used, respectively. The decoupling between translational and rotational dynamics is common for TVC control due to the fact that the attitude of the vehicle can be changed faster than its trajectory [12]. Thus, the TVC-generated force and moment can be expressed in the body-fixed frame by:

$$\begin{aligned} \mathbf{F}_{TVC,B}(t) &= T_{ref}(t) \begin{bmatrix} \cos(\beta_{TVC,y}(t)) \cos(\beta_{TVC,z}(t)) \\ \cos(\beta_{TVC,y}(t)) \sin(\beta_{TVC,z}(t)) \\ -\sin(\beta_{TVC,y}(t)) \end{bmatrix} \\ \mathbf{M}_{TVC,B}(t) &= [\mathbf{x}_{PVP} - \mathbf{x}_{CG}(t)] \times \mathbf{F}_{TVC,B}(t) \end{aligned} \tag{14}$$

with $\mathbf{x}_{PVP} = \begin{bmatrix} x_{PVP} & 0 & 0 \end{bmatrix}^T$ the TVC pivot position.

2.4 Successive convex optimisation guidance algorithm

Convex optimisation consists in transforming the fuel-optimal trajectory problem into a convex one, more precisely into a Second Order Cone Programming (SOCP) problem, which can be solved with efficient solvers in polynomial time. The challenging tasks rely in converting non-convex state and control constraints into the convex form and on the high computational power needed. Recently, the so-called lossless convexification method [15] and the progresses in computational development have enabled to overcome these issues, and therefore to enable real-time trajectory generation in a closed-loop fashion.

Moreover, a particular class of convex optimisation, successive convex optimisation, can be applied to approximate the remaining nonlinearities in the optimal landing problem such as the aerodynamic effects, previously ignored. It consists in iteratively solving convex optimisation SOCP subproblems in which the nonconvex dynamics and constraints are repeatedly linearised using information coming from the previous iteration solution. This algorithm has been first developed by Szmuk *et al.* in Ref. [4] and then adapted in different ways in Refs. [6, 8]. In this paper, the successive convex optimisation algorithm used relies on the work achieved by Guadagnini *et al.* in Ref. [16] where the strategy defined in Ref. [4] was enhanced to be applicable in a closed-loop fashion towards a 6-DoF re-entry dynamics simulator.

For this study, the successive convex optimisation guidance algorithm has been implemented in MATLAB using the CVX library [17] to formulate the convex problems and the ECOS routine [18] to solve them. At each simulation instance defined by the simulation rate, the reference thrust profile $\mathbf{T}_{B,ref}(t)$ and the reference attitude angles

DOI: 10.13009/EUCASS2022-6193

$\{\theta_{ref}(t), \psi_{ref}(t)\}$ are computed from the most recent guidance solution via linear interpolation. Indeed, that solution is stored as an online lookup table which is updated at each guidance step, with the guidance update frequency $f_{gui} = 0.1$ Hz, so every 10 seconds. To enable the formulation of the SOCP subproblems, the optimal control problem must be converted into a finite dimensional parameter optimisation problem. Therefore, the trajectory and optimisation variables are discretised into K uniformly spaced points. At each guidance step, the time vector is divided in that way:

$$t_k = \frac{k-1}{K-1} t_f, \quad k \in [1, K] \tag{15}$$

and because the estimated time of flight $t_f \to 0$ as $t \to ToF$, where ToF is the actual time of flight achieved by the simulation, the accuracy of the discretisation becomes more precised towards the end.

Therefore, to compute the optimal reference trajectory to be followed, several state and control constraints are considered in addition to the re-entry dynamics. Regarding the state constraints, the first one is a lower bound of the mass: for each time instant t_k, $k \in [1, K]$, the mass cannot be lower than the dry mass of the vehicle. This constraint is expressed by:

$$m[k] \geq m_{dry} \tag{16}$$

The second constraint is the so-called glide-slop constraint: it restricts the inertial position to lie within a glide-slope cone with half-angle $\gamma_{gs} \in [0, 90 \text{ deg})$ and vertex at the landing site. This constraint is enforced by:

$$\mathbf{e}_1 \cdot \mathbf{r}_I[k] \geq \tan(\gamma_{gs}) \left\| \begin{bmatrix} \mathbf{e}_2 & \mathbf{e}_3 \end{bmatrix}^T \mathbf{r}_I[k] \right\|_2 \tag{17}$$

where $\mathbf{e}_i$, $i \in [1, 3]$ are the versors. Then, the third constraint concerns the tilt angle, i.e. the angle between the $\mathbf{x}$-axes of the two reference frames, which is bounded to be less than a maximum $\theta_{max} \in [0, 90 \text{ deg})$. It is defined by:

$$\cos(\theta_{max}) \leq \mathbf{e}_{I,1}^T \, \mathbf{R}_I^B[k] \, \mathbf{e}_{B,1} \tag{18}$$

Then, the fourth constraint limits the angular rate of the vehicle, it is enforced by:

$$\|\boldsymbol{\omega}_B[k]\|_2 \leq \omega_{max} \tag{19}$$

Finally, an additional constraint preserves the unit norm of the quaternion, as follows:

$$\|\mathbf{q}_B^I[k]\| = 1 \tag{20}$$

Then, boundary constraints are added regarding initial and desired final conditions. Note that the initial attitude has not been constrained for the first guidance iteration while it was when the problem is solved during the flight to preserve the continuity of the solution. Morevoer, a so-called State-Triggered Constraint (STC) [4] is added. In that case, it consists in imposing an angle of attack α constraint, α_{max}, when the dynamic pressure Q is larger than a prescribed value Q_{max}. This constraint is written in a continuous formulation with a *trigger*-function g_α and a *constraint*-function c_α as follows:

$$\begin{aligned} h_\alpha(\mathbf{r}_I[k], \mathbf{v}_I[k], \mathbf{q}_B^I[k]) &= -\min(g_\alpha(\mathbf{v}_I[k], \mathbf{r}_I[k]), 0) \cdot c_\alpha \leq 0 \\ c_\alpha(\mathbf{v}_I[k], \mathbf{q}_B^I[k]) &= \mathbf{e}_1 \cdot \mathbf{R}_B^I[k] \mathbf{v}_I[k] + \cos(\alpha_{max}) \|\mathbf{v}_I[k]\|_2 \\ g_\alpha(\mathbf{r}_I[k], \mathbf{v}_I[k]) &= Q_{max} - \frac{1}{2}\rho[k] \|\mathbf{v}_I[k]\|_2^2 \end{aligned} \tag{21}$$

Finally, two control constraints are considered to bound the direction and magnitude of the thrust force. The direction is bounded by limiting the TVC up to a maximum gimbal angle δ_{max}. It is enforced by:

$$\cos(\delta_{max}) \|\mathbf{T}_{B,ref}[k]\|_2 \leq \mathbf{e}_1 \cdot \mathbf{T}_{B,ref}[k] \tag{22}$$

Then, the thrust magnitude is bounded between a minimum and maximum values, such as:

$$0 < T_{min} \leq \|\mathbf{T}_{B,ref}[k]\|_2 \leq T_{max} \tag{23}$$

where T_{min} and T_{max} are the lower and upper bounds, respectively.

However, the optimisation problem subjected to the described dynamics and state and control constraints is not convex and must therefore be convexified. In order to do so, the first step is to convert the free-final-time nonlinear continuous-time optimal control problem into an equivalent fixed-final-time nonlinear continuous-time problem. It is achieved in normalising the time of flight from $t \in [0, t_f]$ to $\tau \in [0, 1]$, where τ is the normalised time of flight.

DOI: 10.13009/EUCASS2022-6193

Summarising the nonlinear dynamics as $\dot{\mathbf{x}}(t) = f(\mathbf{x}(t), \mathbf{u}(t))$ with $\mathbf{x}(t) = \begin{bmatrix} m(t) & \mathbf{r}_I^T(t) & \mathbf{v}_I^T(t) & \mathbf{q}_B^I(t)^T & \boldsymbol{\omega}_B^T(t) \end{bmatrix}^T$ the state vector and $\mathbf{u}(t) = \mathbf{T}_{B,ref}(t)$ the control vector, they can be re-written as follows:

$$\dot{\mathbf{x}}(t) = \frac{\mathrm{d}\tau}{\mathrm{d}t}\frac{\mathrm{d}}{\mathrm{d}\tau}\mathbf{x}(t) \tag{24}$$

Therefore, having $\sigma = (\mathrm{d}\tau/\mathrm{d}t)^{-1}$, the normalised nonlinear dynamics are expressed by:

$$\frac{\mathrm{d}}{\mathrm{d}\tau}\mathbf{x}(\tau) = \sigma \cdot f(\mathbf{x}(\tau), \mathbf{u}(\tau)) \tag{25}$$

Then, the nonlinear re-entry dynamics equations, defined in Eqs. (4-6), are discretised and linearised about the solution of the previous iteration, through a first-order Taylor approximation and the nonconvex constraints are convexified. It concerns two state constraints, the norm of the quaternion (Eq. (20)) and the STC (Eq. (21)), and one control contraint, the lower bound of the thrust magnitude (Eq. (23)). The convexification of the Eq. (20) is obtained through a first-order Taylor expansion approximation evaluated about the previous SOCP $(i-1)^{\text{th}}$ iteration:

$$\|\mathbf{q}_B^{I,i-1}[k]\|_2 + \frac{\mathbf{q}_B^{I,i-1}[k]^T}{\|\mathbf{q}_B^{I,i-1}[k]\|_2}(\mathbf{q}_B^{I,i}[k] - \mathbf{q}_B^{I,i-1}[k]) = 1 \tag{26}$$

The same method is used for the STC (Eq. (21)). However, due to the $\min(\cdot)$ function, the constraint is approximated as follows:

$$\begin{cases} h_\alpha(\boldsymbol{\xi}^{i-1}[k]) + \left.\dfrac{\partial h_\alpha}{\partial \boldsymbol{\xi}}\right|_{\boldsymbol{\xi}^{i-1}[k]} (\boldsymbol{\xi}^i[k] - \boldsymbol{\xi}^{i-1}[k]) \leq 0, & \text{if } g_\alpha(\boldsymbol{\xi}^{i-1}[k]) < 0 \\ 0, & \text{otherwise} \end{cases} \tag{27}$$

where $\boldsymbol{\xi}^i[k] = \begin{bmatrix} \mathbf{v}_I^i[k]^T & \mathbf{q}_B^{I,i}[k]^T \end{bmatrix}^T$, $k = \{1, ..., K\}$ is the reference trajectory parameters obtained from the SOCP i^{th} iteration. Lastly, it is applied to the lower bound of the thrust magnitude, obtaining the following expression for $k \in [1, K-1]$:

$$\begin{aligned} h_T(\mathbf{u}[k]) &= T_{min} - \|\mathbf{T}_{B,ref}[k]\|_2 \\ h_T(\mathbf{u}^{i-1}[k]) + \left.\frac{\partial h_T}{\partial \mathbf{u}}\right|_{\mathbf{u}^{i-1}[k]} &(\mathbf{u}^i[k] - \mathbf{u}^{i-1}[k]) \leq 0 \end{aligned} \tag{28}$$

Finally, the successive convex optimisation strategy involves the use of trust regions and virtual controls to prevent artificial unboundedness and artificial infeasibility, respectively. Trust regions implementation allows to limit the deviation between two consecutive iterations. They are defined for state and control vectors but also for the time of flight:

$$\begin{aligned} \|\mathbf{x}^i[k] - \mathbf{x}^{i-1}[k]\|_2 + \|\mathbf{u}^i[k] - \mathbf{u}^{i-1}[k]\|_2 &\leq \Delta^i_{\mathbf{x},\mathbf{u}}[k] \\ \|\sigma^i - \sigma^{i-1}\|_2 &\leq \Delta^i_\sigma \end{aligned} \tag{29}$$

Virtual controls are additional control inputs $\boldsymbol{\nu}^i$ which allows reaching each point of the solution domain, through dynamics relaxation. All that terms must be penalised in the cost function. For the norm $\Delta^i_{\mathbf{x},\mathbf{u}}$ and for the virtual control vector $\boldsymbol{\nu}^i$, it is needed to define an auxiliary variable, respectively S^i_Δ and $S^i_{\boldsymbol{\nu}}$, to avoid a quadratic term in the cost function joined with an inequality constraint [16]. Therefore, the following constraints are added:

$$\begin{aligned} \|\Delta^i_{\mathbf{x},\mathbf{u}}\|_2 &\leq S^i_{\Delta_{\mathbf{x},\mathbf{u}}} \\ \|\boldsymbol{\nu}^i\|_2 &\leq S^i_{\boldsymbol{\nu}} \end{aligned} \tag{30}$$

The objective of the optimal control problem defined is to find the optimal trajectory, subjected to the defined re-entry dynamics and state and control constraints, minimising the vehicle's fuel consumption, which corresponds to maximising the vehicle's final mass. Due to the monotonic behaviour of the propellant consumption with respect to time, the time of flight is selected as the value to be minimised. Therefore, the cost function can be written as follows at each SOCP i^{th} iteration:

$$J = \sigma^i + w_{\boldsymbol{\nu}} S^i_{\boldsymbol{\nu}} + w_\Delta S^i_\Delta + w_{\Delta_\sigma}\Delta^i_\sigma \tag{31}$$

where $w_{\boldsymbol{\nu}}$, w_Δ and w_{Δ_σ} are penalisation weights.

DOI: 10.13009/EUCASS2022-6193

2.5 Gain-scheduled PID controllers

From the reference trajectory computed by the previously defined guidance algorithm and the current states of the vehicle, the control algorithm must be able to generate the necessary commands, in terms of thrust magnitude $T_{ref}(t)$ and deflection angles $\{\beta_{TVC,y}(t), \beta_{TVC,z}(t)\}$, to be applied by the actuators, here the TVC system only, to correct the trajectory of the vehicle. The method adopted here considers the use of two gain-scheduled PID controllers to compute the respective deflection angles. Indeed, the commanded thrust magnitude is directly taken from the guidance algorithm $T_{ref}(t) = \|\mathbf{T}_{B,ref}(t)\|_2$. This approximation is penalised by a low-pass filter which simulates the intrinsic physical of the device and the delay induced is compensated by a PI-controller.

Using a reference trajectory pre-computed offline corresponding to the conditions of the problem studied, the system of equations is linearised and evaluated at the points of the reference trajectory. Thus, the system can be rewritten in terms of perturbed variables $\tilde{\mathbf{x}}(t) = \mathbf{x}(t) - \bar{\mathbf{x}}(t)$ and $\tilde{\mathbf{u}}(t) = \mathbf{u}(t) - \bar{\mathbf{u}}(t)$, where $\bar{\mathbf{x}}(t)$ and $\bar{\mathbf{u}}(t)$ are the reference state and control vectors respectively, to finally obtain:

$$\begin{aligned} \dot{\tilde{\mathbf{x}}}(t) &= \mathbf{A}(t)\tilde{\mathbf{x}}(t) + \mathbf{B}(t)\tilde{\mathbf{u}}(t) \\ \mathbf{y}(t) &= \mathbf{C}(t)\tilde{\mathbf{x}}(t) \end{aligned} \tag{32}$$

where $\mathbf{A}(t) \in \mathbb{R}^{10\times10}$ and $\mathbf{B}(t) \in \mathbb{R}^{10\times3}$ are the Jacobian matrices of the nonlinear equations with respect to the state and control variables respectively, computed with the function `jacobian` in MATLAB, and $\mathbf{C}(t) \in \mathbb{R}^{2\times10}$ enables the extraction of the pitch angle error $\tilde{\theta}(t)$ and the yaw angle error $\tilde{\psi}(t)$.

The problem is then separated into two 3-DoF problems. One is characterised by the motion in the $\mathbf{x}_B\mathbf{z}_B$-plane with the controller on the pitch angle $\theta(t)$ through the deflection angle $\beta_{TVC,y}(t)$. The second problem is characterised by the motion in the $\mathbf{x}_B\mathbf{y}_B$-plane with the controller on the yaw angle $\psi(t)$ through the deflection angle $\beta_{TVC,z}(t)$. An assumption is made on the roll angle ϕ(t) considering it small so that no coupling effects in the dynamics could arise. Therefore, the two linear systems consider the following parameters:

$$\begin{aligned} \mathbf{x}_{pitch}(t) &= \begin{bmatrix} m(t) & v_x(t) & v_z(t) & \omega_y(t) & \theta(t) \end{bmatrix}^T \in \mathbb{R}^5, \quad \mathbf{u}_{pitch}(t) = \beta_{TVC,y}(t), \quad \mathbf{y}_{pitch}(t) = \theta(t) \\ \mathbf{x}_{yaw}(t) &= \begin{bmatrix} m(t) & v_x(t) & v_y(t) & \omega_z(t) & \psi(t) \end{bmatrix}^T \in \mathbb{R}^5, \quad \mathbf{u}_{yaw}(t) = \beta_{TVC,z}(t), \quad \mathbf{y}_{yaw}(t) = \psi(t) \end{aligned} \tag{33}$$

where $v_x(t)$, $v_y(t)$ and $v_z(t)$ are respectively the x, y and z components of $\mathbf{v}_B(t)$, and $\omega_y(t)$, $\omega_z(t)$, respectively the y and z component of $\boldsymbol{\omega}_B(t)$. The corresponding Jacobian matrices are computed in a similar way than for the linear system defined in Eq. (32). This decoupling of the dynamics has been validated in [16].

Due to the time-varying nature of the problem, a single PID controller maybe unable to stabilise the system for the whole trajectory. Therefore, the time of flight has been discretised into 25 slots where the linearisation has been performed. In this way, the problem is divided into regions where it is possible to analyse if the controller is able to stabilise the system. Thanks to that, the controllers can be considered as gain-scheduled PID as the gains can be changed in order to have the desired levels of performance in all the regions. For each system, the gains are tuned with the following performance requirements: an overshoot inferior to 10%, a settling time strictly inferior to 1 s and a phase margin superior to 60 deg. The tuning was performed with the MATLAB application `PID tuner`.

3. Fixed planar fins implementation in the RLV re-entry dynamics simulator

A preliminary assessment of the G&C strategies was carried out in Ref. [13]. It was shown that an enhanced robustness towards perturbations due to external events as well as uncertainties and nonlinearities in the models could be achieved in adding vehicle's control authority. Therefore, the implementation of fixed planar fins will be studied in this subsection.

The implementation of planar fins for G&C strategy was already studied in the literature. Usually two pairs of fins are placed above the vehicle's CG: one pair, $\{\beta_{fin,1}, \beta_{fin,2}\}$, is controlling the motion in the pitch plane while the other, $\{\beta_{fin,3}, \beta_{fin,4}\}$, is controlling the motion in the yaw plane. In Ref. [7], Sagliano *et al.* used aerodynamic coefficients lookup tables which directly consider the state of the vehicle (angle of attack α, sideslip angle β, Mach number Ma) and the fin deflections $\{\beta_{fin,1}, \beta_{fin,2}, \beta_{fin,3}, \beta_{fin,4}\}$. In Ref. [19], they developed a fin model with its corresponding lookup table for the axial coefficient and the derivative of the normal coefficient, only depending on the Mach number. Therefore, the lookup tables are the same for the four fins and the generated force is determined by the fin's local angle of attack defined as functions of the fin deflection and the vehicle's angle of attack or sideslip angle. Finally, in Ref. [12], Simplício *et al.* also developed a fin model but considering only the normal force which is calculated as function of the fin's local angle of attack.

The fin model developed and used is introduced in Sec. 3.1. Then, its implementation in the guidance method and in the RLV re-entry dynamics simulator is presented in Sec. 3.2.

DOI: 10.13009/EUCASS2022-6193

3.1 Fixed planar fins model

As described previously, the vehicle is equipped with four fins working in pairs: one pair is assigned to pitch motion with the deflections $\{\beta_{fin,1}, \beta_{fin,2}\}$ and the other pair to yaw motion with $\{\beta_{fin,3}, \beta_{fin,4}\}$. It is considered that there is not any roll perturbation, meaning that the two pairs always remain in the trajectory yaw and pitch planes, respectively. Table 1 defined the fin positions with its corresponding deflection.

Table 1: Position of the fins' CP with respect to the base of the RLV and corresponding deflections

	Fin 1	**Fin 2**	**Fin 3**	**Fin 4**
Fin CP position $\mathbf{x}_{fin,i}$	$\begin{bmatrix} x_{fin} & yz_{fin} & 0 \end{bmatrix}^T$	$\begin{bmatrix} x_{fin} & -yz_{fin} & 0 \end{bmatrix}^T$	$\begin{bmatrix} x_{fin} & 0 & yz_{fin} \end{bmatrix}^T$	$\begin{bmatrix} x_{fin} & 0 & -yz_{fin} \end{bmatrix}^T$
Fin deflection $\beta_{fin,i}$	$\beta_{fin,1}$	$\beta_{fin,2}$	$\beta_{fin,3}$	$\beta_{fin,4}$

It is further assumed that, due to the reduced fin area compared to the RLV body, only the normal force contribution is considered [12]. Then, the value of normal coefficient of the fin is estimated using lifting-line theory [20]. Knowing that for a symmetric airfoil, the lift coefficient can be approximated by:

$$c_l(\alpha(t)) = 2\pi\alpha(t) \tag{34}$$

To obtain the lift coefficient C_L of the corresponding wing, it is necessary to define the aspect ratio, denoted by AR and defined as

$$AR = \frac{b^2}{S} = \frac{b}{c} \tag{35}$$

where b is the wing span, S is the wing reference area and c is the wing chord. Therefore, the following approximation is obtained [21]:

$$C_L(\alpha(t)) = \left(\frac{AR}{AR+2}\right) c_l(\alpha(t)) \tag{36}$$

This theory is then adapted for the fins of the RLV. Because the flow separation is neglected and the angle of attack of the rocket is around π during the descent, the normal fin coefficient has a sinusoidal dependence on the fin angle of attack $\gamma_{fin,i}(t)$ and can be approximated by:

$$C_{N,fin,i}(\gamma_{fin,i}(t)) = 2\pi\left(\frac{AR_{fin}}{AR_{fin}+2}\right)\sin(\gamma_{fin,i}(t)), \quad i = \{1,2,3,4\} \tag{37}$$

It remains to define the ith fin's angle of attack and its associated force $\mathbf{F}_{fin,i}(t)$ and moment $\mathbf{M}_{fin,i}(t)$ in the vehicle body-fixed reference frame. Figure 1 shows the motion of the vehicle in the pitch plane and from it, it is possible to define:

$$\begin{cases} \gamma_{fin,i}(t) = \beta_{fin,i} - \alpha(t) \\ \mathbf{F}_{fin,i}(t) = \frac{1}{2}\rho(t)\|\mathbf{v}_{air,I}(t)\|_2^2 S_{fin} C_{N,fin,i}(\gamma_{fin,i}(t)) \begin{bmatrix} -\sin(\beta_{fin,i}) & 0 & \cos(\beta_{fin,i}) \end{bmatrix}^T, \quad i = \{1,2\} \\ \mathbf{M}_{fin,i}(t) = [\mathbf{x}_{fin,i} - \mathbf{x}_{CG}] \times \mathbf{F}_{fin,i}(t) \end{cases} \tag{38}$$

where $\alpha(t)$ is the vehicle's angle of attack and S_{fin} is the fin reference area. And similarly, the following formula is obtained in the yaw plane:

$$\begin{cases} \gamma_{fin,i}(t) = -\beta_{fin,i} - \beta(t) \\ \mathbf{F}_{fin,i}(t) = \frac{1}{2}\rho(t)\|\mathbf{v}_{air,I}(t)\|_2^2 S_{fin} C_{N,fin,i}(\gamma_{fin,i}(t)) \begin{bmatrix} \sin(\beta_{fin,i}) & \cos(\beta_{fin,i}) & 0 \end{bmatrix}^T, \quad i = \{3,4\} \\ \mathbf{M}_{fin,i}(t) = [\mathbf{x}_{fin,i} - \mathbf{x}_{CG}] \times \mathbf{F}_{fin,i}(t) \end{cases} \tag{39}$$

where $\beta(t)$ is the vehicle's sideslip angle.

Finally, the total force generated by the fixed planar fins in the inertial reference frame and the total moment generated in the vehicle's body-fixed reference frame are given by:

$$\mathbf{F}_{fins,I}(t) = \mathbf{R}_I^B(t) \sum_{i=1}^{4} \mathbf{F}_{fin,i}(t) \tag{40}$$

$$\mathbf{M}_{fins,B}(t) = \sum_{i=1}^{4} \mathbf{M}_{fin,i}(t) \tag{41}$$

DOI: 10.13009/EUCASS2022-6193

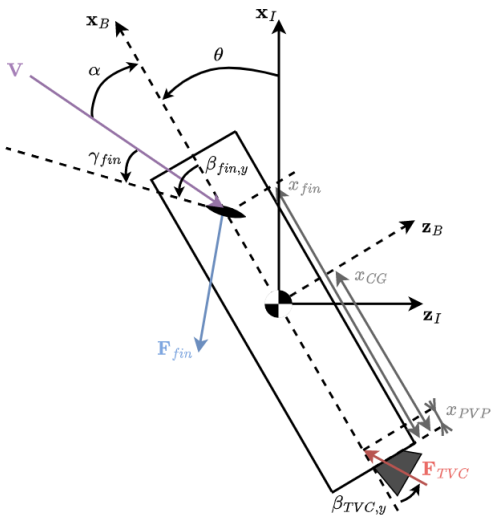

Figure 1: RLV model in the pitch plane

3.2 Implementation in the guidance strategy and in the RLV re-entry dynamics simulator

From the previously defined fixed planar fins model, the equations of motion introduced in Eqs. (4-6), are enhanced and updated in the RLV re-entry dynamics simulator as follows:

$$\begin{cases} \dot{m}(t) = -\dfrac{\|\mathbf{F}_{TVC,I}(t)\|_2}{I_{sp}g_0} - \dfrac{A_{nozzle}P_{amb}(t)}{I_{sp}g_0} \\ \dot{\mathbf{r}}_I(t) = \mathbf{v}_I(t) \\ \dot{\mathbf{v}}_I(t) = \dfrac{1}{m(t)}\left[\mathbf{F}_{TVC,I}(t) + \mathbf{F}_{aero,I}(t) + \mathbf{F}_{fins,I}(t)\right] + \mathbf{g}_I(t) \\ \dot{\mathbf{q}}_B^I(t) = \dfrac{1}{2}\begin{bmatrix} q_4(t) & -q_3(t) & q_2(t) \\ q_3(t) & q_4(t) & -q_1(t) \\ -q_2(t) & q_1(t) & q_4(t) \\ -q_1(t) & -q_2(t) & -q_3(t) \end{bmatrix}\boldsymbol{\omega}_B(t) \\ \dot{\boldsymbol{\omega}}_B(t) = J^{-1}(t)\left[\mathbf{M}_{TVC,B}(t) + \mathbf{M}_{aero,B}(t) + \mathbf{M}_{fins,B}(t) - \boldsymbol{\omega}_B(t) \times J\boldsymbol{\omega}_B\right] \end{cases} \tag{42}$$

The vehicle's angle of attack and sideslip angle are obtained from the air-relative velocity expressed in the vehicle's body-fixed reference and are defined by:

$$\alpha(t) = \text{atan2}(v_{air,B,z}(t), v_{air,B,x}(t)) \tag{43}$$

$$\beta(t) = \arcsin\left(\frac{v_{air,B,y}(t)}{\|\mathbf{v}_{air,B}(t)\|}\right) \tag{44}$$

In what concerns the guidance strategy, the nonlinear re-entry dynamics equations, defined in Eq. (42), are discretised and linearised about the solution of the previous iteration, through a first-order Taylor approximation, following the scheme achieved in Sec. 2.4, but adding the fins-generated force and moment.

4. Simulation results

This section illustrates the results obtained with the proposed G&C architecture coupled with the RLV re-entry dynamics simulator with and without fins implementation (Sec. 4.1). Then, a sensitivity analysis is carried out to assess the impact of specific parameters on the obtained trajectory (Sec. 4.2).

4.1 Comparison of results without fins and with fins for one specific scenario

In order to assess the impact of the fins, a specific scenario with and without fins have been tested. The initial and final conditions are described in Tables 2a and 2b, respectively. The parameters regarding the fins implementation are

DOI: 10.13009/EUCASS2022-6193

summarized in Table 2c. The initial conditions of the case studied allows to study the impact of fins for a trajectory evolving mainly in the pitch plane. Other simulations have also been carried out for a trajectory mainly in the yaw plane and for a trajectory in both planes and showed similar results, therefore they are not displayed in this paper. Note that for this simulation, no wind is considered.

Table 2: Initial, final conditions and fins model parameters

(a) Initial conditions

Parameter	Value
$\mathbf{r}_I[0]$	$[25 \;\; 0 \;\; -12]^T$ km
$\mathbf{v}_I[0]$	$[-850 \;\; -50 \;\; 700]^T$ m/s
$\boldsymbol{\omega}_B[0]$	$[0 \;\; 0 \;\; 0]^T$ rad/s
m_0	12,000 kg

(b) Final conditions

Parameter	Value
$\mathbf{r}_I[K]$	$[0 \;\; 0 \;\; 0]^T$ km
$\mathbf{v}_I[K]$	$[-5 \;\; 0 \;\; 0]^T$ m/s
$\boldsymbol{\omega}_B[K]$	$[0 \;\; 0 \;\; 0]^T$ rad/s
$\mathbf{q}_B^I[K]$	$[0 \;\; 0 \;\; 0 \;\; 1]^T$

(c) Fins model parameters

Parameter	Value	Unit
x_{fin}	11.1	m
yz_{fin}	2.5	m
b_{fin}	1.2	m
c_{fin}	0.8	m
S_{fin}	0.96	m^2
AR_{fin}	1.5	–
$\beta_{fin,i}$	0	deg

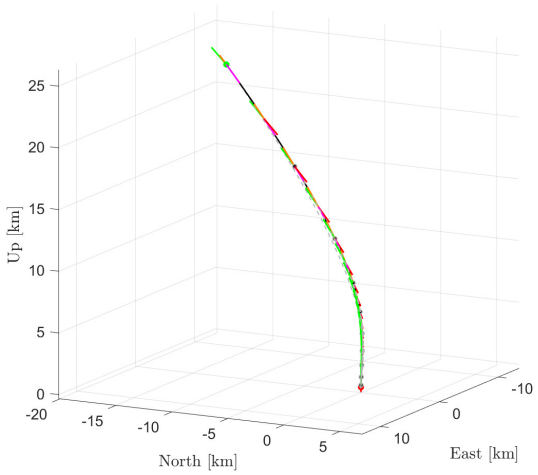

(a) Trajectory of the RLV without fins

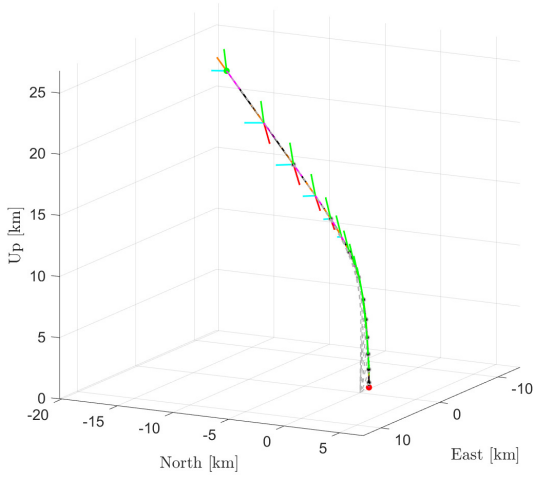

(b) Trajectory of the RLV with fins

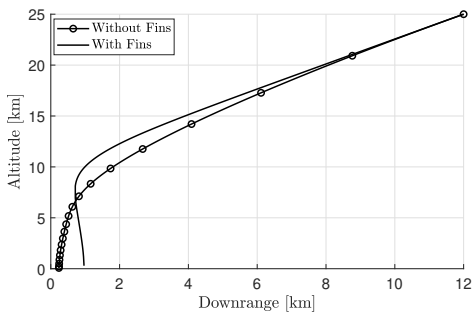

(c) Altitude vs. downrange

Legend

Propagated Trajectory	
Computed Reference Trajectories	
Vertical Body Axis ($\mathbf{R}_I^B\mathbf{e}_1$)	
Inertial Velocity ($\mathbf{v}_I$)	
Thrust ($\mathbf{T}_I$)	
Aerodynamic Force ($\mathbf{F}_{aero,I}$)	
Fins Aerodynamic Force ($\mathbf{F}_{fins,I}$)	
Pitch Fins Vertical Body Axis ($\mathbf{R}_I^B\mathbf{R}_B^{F_y}\mathbf{e}_1$)	
Initial State	
Final State	
Temporal Node	

Figure 2: Comparison of RLV re-entry trajectories without fins and with fins

Figure 2 shows the converged trajectory for the case without fins and the case with fins, and a comparison of their altitude versus downrange profile. The temporal nodes which represent the moment when the guidance algorithm is executed, i.e. when a new reference trajectory is computed, are displayed. Moreover, the forces acting on the vehicle as well as the vertical axes of the vehicle and fins are represented at different times of the descent. From this simulation, it is clear that the aerodynamic forces are always anti-parallel to the velocity vector and are therefore interpreted as

DOI: 10.13009/EUCASS2022-6193

drag forces (see Eq. (7)). For the case without fins in Figure 2a, it implies that the commanded thrust vector is nearly anti-parallel to the velocity vector to counteract the aerodynamic drag. For the case with fins in Figure 2b, the attitude of the rocket coupled with the trajectory lead to the creation of an aerodynamic force generated by the fins controlling the pitch motion. Therefore, in that case the commanded thrust vector is modified accordingly. Note that the initial attitude of the vehicle $\mathbf{q}_B^I[0]$ is not constrained, therefore the guidance algorithm finds different initial reference optimal trajectories in terms of attitude. Finally, fins lead to a larger downrange error (see Figure 2c) more likely due to the lack of control authority from the TVC to correct the deviation caused by their addition.

4.2 Sensitivity analysis

In this section, the fins model parameters displayed in Table 2c are modified independently in order to study their impact on the generated RLV re-entry trajectory. Moreover, wind is added in the simulator and fin deflections are modified accordingly to counteract the induced deviations. This study enables to demonstrate how the addition of fins can increase the control authority of the vehicle and therefore increase its robustness towards disturbances and uncertainties.

4.2.1 Fin deflections

For this study, several fin deflections configurations have been applied to the vehicle and are compared in Figure 3. Assuming perfect roll attitude control, it is considered that $\beta_{fin,1} = \beta_{fin,2} = \beta_{fin,y}$ and $\beta_{fin,3} = \beta_{fin,4} = \beta_{fin,z}$.

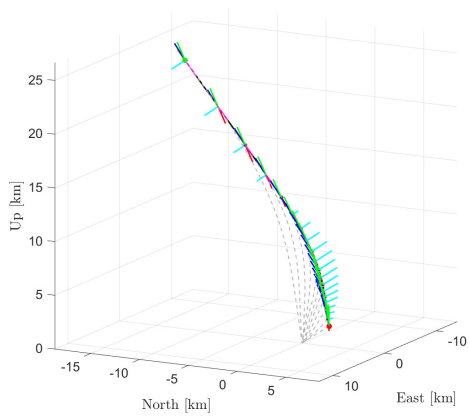

(a) Trajectory of the RLV with $\beta_{fin,y} = -10$ deg and $\beta_{fin,z} = 0$ deg

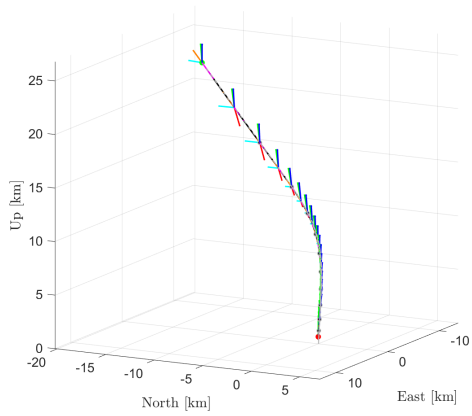

(b) Trajectory of the RLV with $\beta_{fin,y} = 5$ deg and $\beta_{fin,z} = 0$ deg

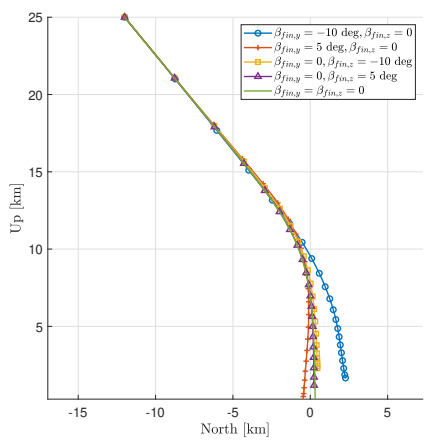

(c) Trajectories in the pitch plane

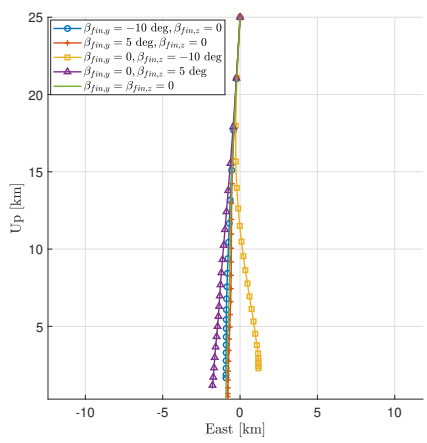

(d) Trajectories in the yaw plane

Figure 3: Comparison of RLV re-entry trajectories with different fin deflections configurations

From this figure, the effect of fin deflections is clear. A negative fin deflection of the fins controlling the pitch motion leads to a positive downrange error towards the North while a positive fin deflection of the same fins leads to

DOI: 10.13009/EUCASS2022-6193

a negative downrange error. Figures 3a and 3b illustrate this statement showing also the attitude of the vehicle during the re-entry and the forces involved. Figure 3c confirms that a fin deflection of $\{\beta_{fin,1}, \beta_{fin,2}\}$ enables the motion in the pitch plane. Figure 3d draws the same conclusions for a deflection of $\{\beta_{fin,3}, \beta_{fin,4}\}$ regarding the yaw motion.

4.2.2 Fin positions

The position of the fins in the longitudinal axis of the RLV, x_{fin}, is a critical parameter involved in the level arm generating the fin-induced aerodynamic moment. Figure 4 shows the RLV re-entry trajectories for different fin positions. From Figure 4a showing the different trajectories in the pitch plane, it is possible to see that the final trajectory is quite sensitive to this parameter. Indeed, the fins aerodynamic forces generated (Figure 4b) fluctuates due to different reference trajectory computations. Moreover, as it is illustrated in Figure 4c and proved by Eq. (38, 39), the higher is the fin in the vehicle's longitudinal axis, the more is the fin-induced aerodynamic moment, therefore the more is the available control authority. Finally, this parameter also affects the time of flight and therefore the fuel consumption, therefore a trade-off must be carried out as a high fin position induces a longer time of flight.

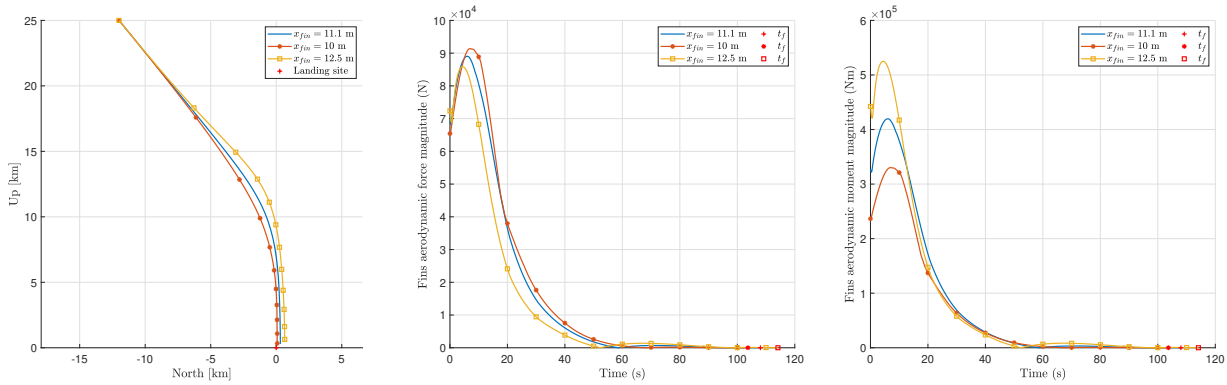

(a) Trajectories in the pitch plane (b) Fins aerodynamic force magnitude (c) Fins aerodynamic moment magnitude

Figure 4: Comparison of RLV re-entry trajectories with different fin positions

4.2.3 Fin dimensions

In this study, the dimensions of the fins have been modified. It implies the fin span b_{fin} and the fin chord c_{fin}, and therefore the fin aspect ratio AR_{fin} and its reference area S_{fin}. Three cases have been tested and the results are displayed in Figure 5; in the first one, the fin span is increased by 10%, in the second one, the fin chord is increased by 10%, and in the last case, both fin span and chord are increased by 10%. As for the fin positions, a trade-off must be achieved to choose the best parameters. A higher aspect ratio increases the available control authority (Figure 5c) and enables better performance (Figures 5a-5b). Higher fin reference area shows enhanced control authority but can cause instabilities at

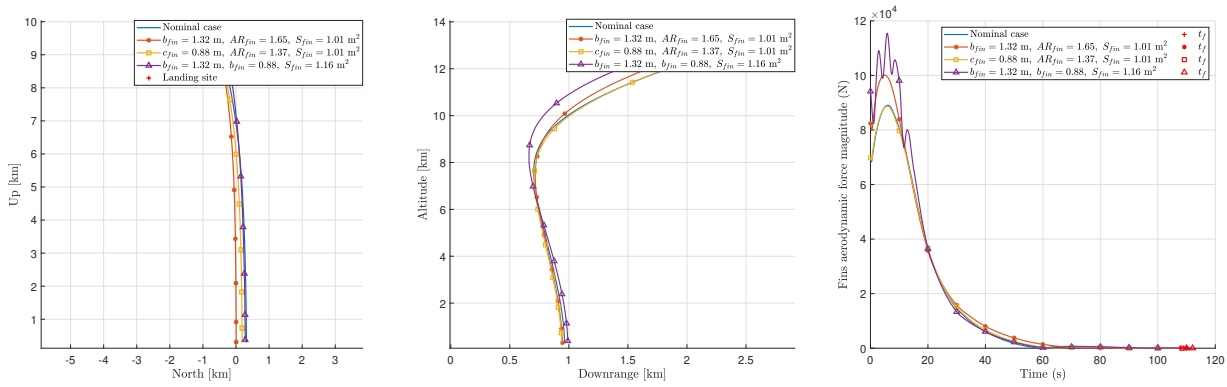

(a) Trajectories in the pitch plane (zoomed) (b) Altitude vs. downrange (zoomed) (c) Fins aerodynamic force magnitude

Figure 5: Comparison of RLV re-entry trajectories with different fin dimensions

DOI: 10.13009/EUCASS2022-6193

the beginning of the flight (Figure 5c).

4.2.4 Wind

In this study, wind has been added to the simulator. Retrieving Eqs. (2,3), the amplitude of the gust has been defined as $\mathbf{A}_{gust} = \begin{bmatrix} 14 & 14 & 14 \end{bmatrix}^T$ m/s from an altitude of $11,000$ m to $2,000$ m. Figure 6 compares two simulations with wind conditions: one without fin deflection, the other with 5 deg deflection of the fins controlling the pitch motion to counteract the deviation induced by the wind. Looking at the trajectory in the pitch plane (Figure 6a) and the downrange error (Figure 6b), it is clear that the case with fin deflections shows better performance and therefore demonstrates that the addition of fin control authority is relevant to counteract disturbances.

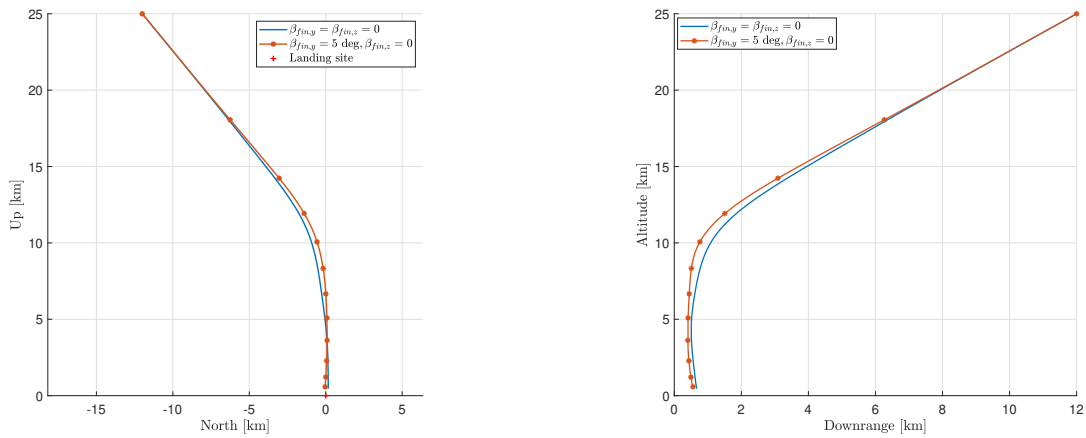

(a) Trajectories in the pitch plane

(b) Altitude vs. downrange

Figure 6: Comparison of RLV re-entry trajectories with wind conditions

5. Conclusions

This paper presents a RLV re-entry dynamics simulator with closed-loop guidance and control integration, from design, to validation and critical discussion on some representative simulation cases. This simulator covers a VTVL first-stage booster atmospheric re-entry and soft pinpoint landing. It includes the 6-DoF re-entry dynamics of a rigid-body model with varying mass, evolving in the terrestrial atmosphere with varying environmental parameters, uncertainties and disturbances, and subjected to external forces. To steer the spacecraft towards a controlled atmospheric re-entry and a soft pinpoint landing, the vehicle is equipped with a TVC system controlled by gain-scheduled PID controllers, which correct the trajectory deviations with respect to the reference profile generated by a successive convex optimisation guidance algorithm. In addition to this, to enhance the RLV control authority during the atmospheric re-entry, the insertion of two pairs of planar fins for increased aerodynamic effectiveness is particularly studied and their impact on the vehicle's trajectory is analysed.

Several simulations case studies are presented, each illustrating one modification in a sensitive parameter of the fins model implemented, affecting the vehicle's final trajectory. Numerical results and vehicle's behaviour confirmed that the proposed planar fins model is viable to assess G&C strategies for RLV atmospheric re-entry. There are several lessons learned from this study. The first is that a significant vehicle's control authority can be provided by planar fins compared to TVC, especially at high altitude where the gravity is not predominant, and particularly to counteract disturbances such as wind. The second aspect is that fixed fins implementation lead to deviations from the reference trajectory computed by the guidance algorithm. Therefore, the control of TVC gimbal angles with gain-scheduled PID controllers is not robust enough to compensate accelerations and uncertainties coming from fin aerodynamics. Future extensions of this work will implement a more robust control method considering TVC and moveable fins as actuators.

6. Acknowledgments

The project leading to this application has received funding from the European Union's Horizon 2020 research and innovation programme under the Marie Skłodowska-Curie grant agreement No 860956.

DOI: 10.13009/EUCASS2022-6193

References

[1] Elisabeth Howell. *SpaceX: Facts about Elon Musk's private spaceflight company*. Space.com. 2022. URL: https://www.space.com/18853-spacex.html. (Retrieval Date: 23-May-2022).

[2] Blue Origin. *New Glenn: Our next (really) big step - an orbital reusable launch vehicle that will build the road to space*. URL: https://www.blueorigin.com/new-glenn. (Retrieval Date: 23-May-2022).

[3] Daniel P. Scharf et al. "Implementation and Experimental Demonstration of Onboard Powered-Descent Guidance". *Journal of Guidance, Control, and Dynamics* 40.2 (Feb. 2017), pp. 213–229. DOI: 10.2514/1.g000399.

[4] Michael Szmuk, Taylor P. Reynolds, and Behçet Açıkmeşe. "Successive Convexification for Real-Time Six-Degree-of-Freedom Powered Descent Guidance with State-Triggered Constraints". *Journal of Guidance, Control, and Dynamics* 43.8 (Aug. 2020), pp. 1399–1413. DOI: 10.2514/1.g004549.

[5] Marco Sagliano. "Pseudospectral Convex Optimization for Powered Descent and Landing". *Journal of Guidance, Control, and Dynamics* 41.2 (Feb. 2018), pp. 320–334. DOI: 10.2514/1.g002818.

[6] Xinfu Liu. "Fuel-Optimal Rocket Landing with Aerodynamic Controls". *Journal of Guidance, Control, and Dynamics* 42.1 (Jan. 2019), pp. 65–77. DOI: 10.2514/1.g003537.

[7] Marco Sagliano et al. "Onboard Guidance for Reusable Rockets: Aerodynamic Descent and Powered Landing". *AIAA Scitech 2021 Forum*. American Institute of Aeronautics and Astronautics, Jan. 2021. DOI: 10.2514/6.2021-0862.

[8] Pedro Simplício, Andrés Marcos, and Samir Bennani. "Guidance of Reusable Launchers: Improving Descent and Landing Performance". *Journal of Guidance, Control, and Dynamics* 42.10 (Oct. 2019), pp. 2206–2219. DOI: 10.2514/1.g004155.

[9] Erwin Mooij. *Linear quadratic regulator design for an unpowered, winged re-entry vehicle*. 08 Astrodynamics and Satellite Systems 03. Delft University Press, 1998. ISBN: 9040715971.

[10] Diego Navarro-Tapia et al. "Structured H-infinity and Linear Parameter Varying Control Design for the VEGA Launch Vehicle". Proceedings of the 7th European Conference for Aeronautics and Space Sciences. Milano, Italy, 3-6 July 2017, 2017. DOI: 10.13009/EUCASS2017-257.

[11] Marco Sagliano et al. "Robust Control for Reusable Rockets via Structured H-infinity Synthesis". Proceedings of the 11th International ESA Conference on Guidance, Navigation & Control Systems. Virtual Event, 22-25 June 2021, 2021.

[12] Pedro Simplício, Andrés Marcos, and Samir Bennani. "Reusable Launchers: Development of a Coupled Flight Mechanics, Guidance, and Control Benchmark". *Journal of Spacecraft and Rockets* 57.1 (Jan. 2020), pp. 74–89. DOI: 10.2514/1.a34429.

[13] Alice De Oliveira and Michèle Lavagna. "Reusable Launch Vehicles Re-entry: Preliminary Architecture towards Optimal Guidance and Robust Control". Proceedings of the XXVI International Congress of the Italian Association of Aeronautics and Astronautics (AIDAA). On-line event hosted by the Tuscany AIDAA Section in Pisa, 31 August - 3 September 2021, 2021.

[14] *MATLAB Aerospace Toolbox User's Guide*. Tech. rep. MathWorks, Natick, MA, 2017.

[15] Behçet Açıkmeşe and Scott R. Ploen. "Convex Programming Approach to Powered Descent Guidance for Mars Landing". *Journal of Guidance, Control, and Dynamics* 30.5 (Sept. 2007), pp. 1353–1366. DOI: 10.2514/1.27553.

[16] Jacopo Guadagnini, Michèle Lavagna, and Paulo Rosa. "Model predictive control for reusable space launcher guidance improvement". *Acta Astronautica* (Oct. 2021). DOI: 10.1016/j.actaastro.2021.10.014.

[17] Michael Grant and Stephen Boyd. *CVX: Matlab Software for Disciplined Convex Programming, version 2.1*. http://cvxr.com/cvx. Mar. 2014.

[18] Alexander Domahidi, Eric Chu, and Stephen Boyd. "ECOS: An SOCP solver for embedded systems". *2013 European Control Conference (ECC)*. IEEE, July 2013. DOI: 10.23919/ecc.2013.6669541.

[19] Marco Sagliano et al. "Booster Dispersion Area Management through Aerodynamic Guidance and Control". *AIAA SCITECH 2022 Forum*. American Institute of Aeronautics and Astronautics, Jan. 2022. DOI: 10.2514/6.2022-0759.

[20] John Anderson. *Fundamentals of Aerodynamics*. Sixth Edition. McGraw-Hill Education, 2017. ISBN: 9781259129919.

[21] Robert C. Nelson. *Flight Stability and Automatic Control*. McGraw-Hill Education, 1989. ISBN: 0070462186.